Mineral–water reactions in Earth's mantle: Predictions from Born theory and *ab initio* molecular dynamics

Sarah J. Fowler [a,*], David M. Sherman [a], John P. Brodholt [b], Oliver T. Lord [a]

[a] *School of Earth Sciences, University of Bristol, Queen's Rd., Bristol BS8 1RJ, UK*
[b] *Department of Earth Sciences, University College London, Gower St., London WC1E 6BT, UK*

ARTICLE INFO

ABSTRACT

Recent studies present compelling evidence that a free aqueous fluid phase exists within the upper mantle. Fluid may be present at depths as great as the transition zone (410–660 km) and possibly beyond. The chemical reactivity of such deep fluids can be predicted from the Born model of solvation. To use the Born model, we need to know the dielectric constant of water under mantle conditions. We have used *ab initio* molecular dynamics simulations to determine the dielectric constant of water up to a pressure of 30 GPa and a temperature of 3000 K. Increased temperature lowers the dielectric constant and decreases ion solvation, but pressure overcomes this effect. The resulting high dielectric constant suggests that aqueous mantle fluids are highly reactive for ion solvation and mineral dissolution. We tested this by using the Helgeson–Kirkham–Flowers equation of state to estimate free energies of several mineral-solution and ion solvation reactions under mantle conditions. The results support previous estimates of carbonate solubility in the mantle. We also find that mantle fluids may play a key role in transporting ore metals: we evaluated the solubility of chalcopyrite and the complexation of Cu and Fe by Cl under mantle conditions and find that metal complexation is as significant as in ore-forming fluids in the crust. At reasonable conditions of pH and f_{H_2}, chalcopyrite is highly soluble. We tentatively hypothesize that exsolved fluids from subducted slabs may extract and mobilize primary sulfides in the mantle, implying potentially deep sources for porphyry copper deposits.

1. Introduction

Reactions between minerals and aqueous fluids have played a central role in the chemical differentiation of the Earth. This is most easily observed in the continental crust and in the formation of hydrothermal ore deposits. It has long been assumed that mineral-solution reactions are not relevant to the chemistry of the Earth's mantle. However, emerging evidence of aqueous fluids in the Earth's mantle implies that such reactions also occur at depths beyond the Moho.

The bulk upper mantle is relatively dry due to the limited water storage capacity of its dominant minerals. This, in combination with electrical conductivity data, implies an average water concentration of only 0.01 wt% H_2O (Karato, 2011; Khan and Shankland, 2012; Ohtani, 2020). However, water contents can be elevated locally. Within subducting slabs, hydrous minerals break down as pressure and temperature (P, T) increase, liberating aqueous fluids (e.g., Schmidt and Poli, 2003; 2013). The depth and mass of fluid release depends on P, T and slab composition. A subducting slab typically has 1–2 wt% water bound

within hydrous phases, of which two thirds may dehydrate before the slab reaches a depth of 240 km (van Keken et al., 2011).

There is a range of recent evidence for fluids in the upper mantle. For example, at the Cascadia subduction zone, USA, a broad (50 to 80 km) wedge-shaped region of cold and partially serpentinized shallow mantle is a likely product of reaction between aqueous fluids from the subducting slab and surrounding mantle rocks during upward transport. Subsequent dehydration of the serpentinite may be associated with >25 Myr of water release into the overlying crust that hosts the San Andreas Fault system (Kirby et al., 2014), where a deep mantle source of pressurized water has long been hypothesized to facilitate slip (e.g., Irwin and Barnes, 1975; Zoback et al., 1987; Zoback et al., 1993; Rice, 1992; Hickman et al., 1995; Faulkner and Rutter, 2001; Thomas et al., 2009). In the Western Alps across the Switzerland–Italy border, Bovay et al. (2021) describe evidence for pervasive fluid–rock interaction within a subducting slab in the form of low-$\delta^{18}O$ garnet metasomatized by fluid derived from breakdown of the assemblage antigorite + brucite. Earthquake swarms beneath the Mariana, Izu-Bonin, and Cascadia arc

systems delineate conduits that transport aqueous fluid and/or fluid-fluxed melt from the dehydrating slab to volcanic centers at the surface (White et al., 2019; McGary et al., 2014). The best-resolved earthquake swarm, beneath the Mariana arc, defines an approximately vertical pipe-like structure of ~50 km diameter that extends to at least 250 km depth, where it intersects the surface of the subducting Pacific slab (White et al., 2019). The earthquakes may occur a further few tens of km downward into the slab. The limited duration of the swarms implies that associated fluids/melts flow rapidly upward through the mantle wedge, at rates of km/hr or faster.

Geophysical studies provide wide-ranging estimates of transition zone water content. At one extreme, electrical conductivity (Karato, 2011) and seismological data (Li et al., 2013; Suetsugu et al., 2006; Wang et al., 2019) support high (up to ~1 wt%) water concentrations, possibly even free water (Karato et al., 2020). However, Zhang et al. (2021) found from Fe–Mg interdiffusion experiments that ~0.1–0.5 wt% structurally bound H_2O is sufficient to account for high conductivity values in the upper part (410–520 km) of the transition zone. Whatever the case, studies of inclusions in mantle-derived diamonds support the suggestion that the transition zone is at minimum *locally* hydrated, potentially to the point of saturation. Pearson et al. (2014) reported a single hydrous ringwoodite inclusion within a diamond where the water content approaches the solubility limit (1.5 wt%). Ice-VII inclusions in diamonds from the transition zone (and possibly the lower mantle) suggest that local saturation generates free aqueous fluid (Tschauner et al., 2018; Ohtani, 2020). Palot et al. (2016) interpreted brucite within ferropericlase inclusions in superdeep diamonds as having precipitated from H_2O-bearing fluid trapped during diamond formation in the uppermost lower mantle. Hydrocarbon (C–H), hydrogen (H_2), and CH_4-rich fluid inclusions in transition zone diamonds may represent fluids released under reducing conditions. Such fluids might become oxidized on ascent due to an increase in oxygen fugacity with decreasing depth in the mantle (Das et al., 2017). Diamonds themselves may crystallize from fluids released at depths as great as ~300–700 km during subduction, a phenomenon that has been invoked to explain deep seismicity (Shirey et al., 2021).

A hydrous transition zone may supply H_2O to the surrounding mantle at its upper and lower boundaries via the transition of hydrous wadsleyite to water-poor olivine (in the upper mantle) or the transition of hydrous ringwoodite to water-poor bridgmanite + ferropericlase (in the lower mantle). In these regions, the presence of aqueous fluid may generate hydrous silicate melt (Hirschmann, 2006; Panero et al., 2020). Recent *ab initio* molecular dynamics simulations of likely melt compositions within the MgO–SiO_2–H_2O system under deep upper mantle to shallow lower mantle conditions (Drewitt et al., 2022) suggest that such melts would be positively buoyant, highly inviscid, and therefore highly mobile, should transportation pathways exist.

Similar to the upper mantle, current data suggest that the major minerals of the lower mantle have minimal water storage capacity (Karato et al., 2020). However, dense hydrous magnesium silicates may survive into the lower mantle within subducted slabs (Faccenda, 2014) and stishovite, a major phase within subducted oceanic crust, can contain weight-percent levels of water (Lin et al., 2020). This implies that fluid may be released even within the lower mantle (Hirschmann, 2006; Schmandt et al., 2014; Ohtani, 2020; Gu et al., 2022). However, there are few constraints on its distribution and fate (Karato et al., 2020).

Given the potential for free aqueous fluids within the mantle, albeit local, a key question is how such fluids would react with mantle minerals and dissolve ions. At a molecular level, water solvation properties result from electrostatic attraction between the dipole moments of individual water molecules and ions in solution. At a macroscopic level, a solvent made of individual dipoles can be modelled as a continuum with a dielectric constant. The Born model of solvation (Born, 1920) predicts the free energy of solvation, $\Delta \overline{G}_{s,j}^{o}$, as a function of the solvent dielectric
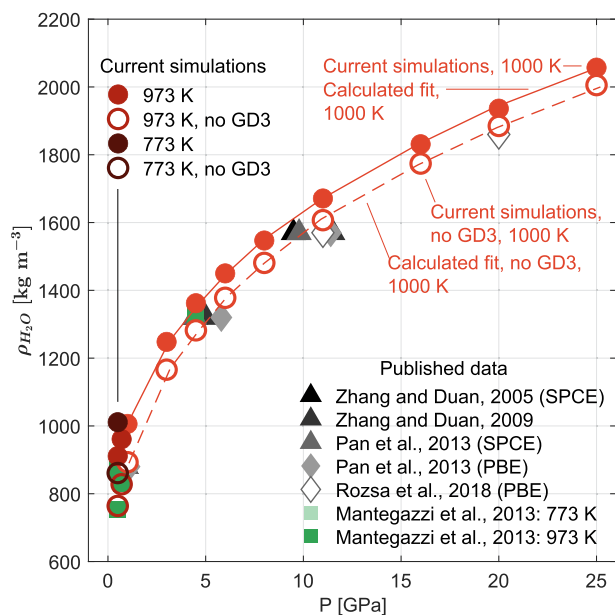

Fig. 1. Comparison of calculated densities from our CP2K PBE, NPT-ensemble *ab initio* molecular dynamics simulations with data from the literature. Here and elsewhere, open and filled circles signify exclusion ("no GD3" in legend) and inclusion, respectively, of Grimme's D3 dispersion correction. Green squares represent results based on an equation of state extrapolated from measurements to 4.5 GPa and 673 K (Mantegazzi et al., 2013). Data from Zhang and Duan (2009) represent a model for C—O—H fluid in the mantle that is based on an equation of state, statistical mechanics results, and non-stoichiometric global free-energy minimization. Other plotted data represent results from *ab initio* and classical molecular dynamics simulations that, as far as we know, do not include correction for dispersion. Calculated density for all simulations is tabulated in Table 1. Fig. S1 (supplementary material) displays P vs. ρ at selected T (800, ~1000, 2000, and 3000 K).

constant and the Born coefficient, ω_j, of the dissolved species, *j*:

$$\Delta \overline{G}_{s,j}^{o} = \omega_j \left(\frac{1}{\varepsilon} - 1 \right)$$

The dielectric constant of water decreases with increasing T as thermally induced rotational disorder breaks down the alignment of the dipole moments of water molecules in the presence of an electric field (e.g., a charged ion). Accordingly, at high T, we expect solvation to be less favorable. However, P increases the dielectric constant as it restricts the rotational motion of water molecules. In addition, but less importantly, thermally induced vibrational motions induce changes in the molecular dipole moment via the O—H bond length and H—O—H bond angle by influencing the strength of hydrogen bonds (Chen et al., 2003; Chaplin, 2007). A P- and T-dependent Born model has been implemented in the Helgeson–Kirkham–Flowers equations of state (HKF; Helgeson et al., 1981; Tanger and Helgeson, 1988; Shock et al., 1992; Sverjensky et al., 2014) to estimate Gibbs free energies of solvation of aqueous species at elevated P and T. The accuracy of these models depends on the accuracy of the dielectric constant of water, ε.

Experimental measurements of ε extend only to 0.5 GPa and 823 K (Heger et al., 1980) and so a number of studies have extrapolated ε to higher P, T. For instance, an equation of state for ε, based on estimates from the literature and the Kirkwood equation, is routinely used to extend the maximum P, T to 1.2 GPa and ~873 K, respectively (Fernández et al., 1995; Fernández et al., 1997; standard formulation of the International Association for the Properties of Water and Steam, IAPWS, 1997). Pan et al. (2013) used an alternative approach of *ab initio* molecular dynamics simulation to calculate ε at five P, T state points, 1.1, 5.8, and 11.4 GPa at 1000 K and 5.2 and 8.9 GPa at 2000 K. Most

Table 1
Dielectric constant and density values from *ab initio* simulations.

T [K]	P [GPa]	$^{\dagger}\rho$ [kg m^{-3}]	$^{\ddagger}\rho$ [kg m^{-3}]	$^{\dagger}\varepsilon$	$^{\ddagger}\varepsilon$
773	0.3	795	960	17	21
773	0.5	861	1011	18	23
823	0.5	834	987	16	21
973	0.5	764	911	11	14
973	0.7	828	961	13	16
800	1	967	1092	20	24
800	3	1218	1307	31	35
800	4.5	1330	1412	38	42
800	6	1422	1495	44	46
800	8	1522	1591	53	53
800	11	1645	1710	61	68
1000	1	893	1006	14	16
1000	3	1166	1248	21	24
1000	4.5	1282	1362	25	28
1000	6	1378	1450	30	35
1000	8	1481	1547	36	45
1000	11	1607	1671	51	56
1000	16	1774	1831	62	68
1000	20	1883	1936	71	73
1000	25	2004	2057	74	76
1500	0.5	569	672	4	5
1500	1	745	831	6	7
1500	4.5	1185	1259	14	17
1500	6	1287	1358	19	22
1500	8	1397	1460	25	30
1500	11	1530	1591	35	40
1500	16	1702	1760	46	47
1500	20	1816	1869	50	51
1500	25	1937	1987	53	55
1500	30	2043	2091	57	57
2000	1	638	711	4	4
2000	4.5	1104	1173	10	12
2000	6	1216	1278	14	17
2000	8	1330	1393	21	26
2000	11	1470	1530	29	32
2000	16	1649	1700	37	38
2000	20	1764	1818	39	40
2000	25	1886	1934	42	43
2000	30	1993	2039	44	45
2273	1	583	656	3	3
2273	3	929	994	6	8
2273	4.5	1069	1133	8	12
2273	6	1180	1243	13	16
2273	8	1299	1360	20	24
2273	10	1397	1455	24	28
2273	20	1738	1788	36	37
2273	30	1969	2015	40	40
3000	0.5	325		2	
3000	1	497	540	2	2
3000	3	840		5	
3000	4.5	995	1049	10	11
3000	6	1105	1166	14	16
3000	8	1231	1286	19	20
3000	11	1379	1431	23	24
3000	20	1682	1728	28	29
3000	25	1804	1850	30	31
3000	30	1912	1956	32	32

ρ, (density) and ε (dielectric constant) based on 110 water molecules and CP2K's QUICKSTEP module for *ab initio* simulation. All simulations used the PBE exchange–correlation functional without (†) and with (‡) Grimme's dispersion correction. Predictions are based on CP2K cutoff and relative cutoff values of 1000 Ry and 60 Ry, respectively. Values are rounded to the nearest integer.

recently, Sverjensky et al. (2014) extended the HKF equations of state to 6 GPa and 1473 K, predicting ε based on an expression from statistical mechanics for ε of a hard-sphere fluid (Franck et al., 1990). The revised HKF equations of state are presented along with revised predictive correlations for the estimation of equation of state coefficients in the Deep Earth Water (DEW) model (Sverjensky et al., 2014). This involved first calibrating the expression to experimental data from Heger et al. (1980) at 573 to 823 K, estimates from the literature analysis of Fernández et al. (1997) to 2.5 GPa, and data from Pitzer (1983) at 873,
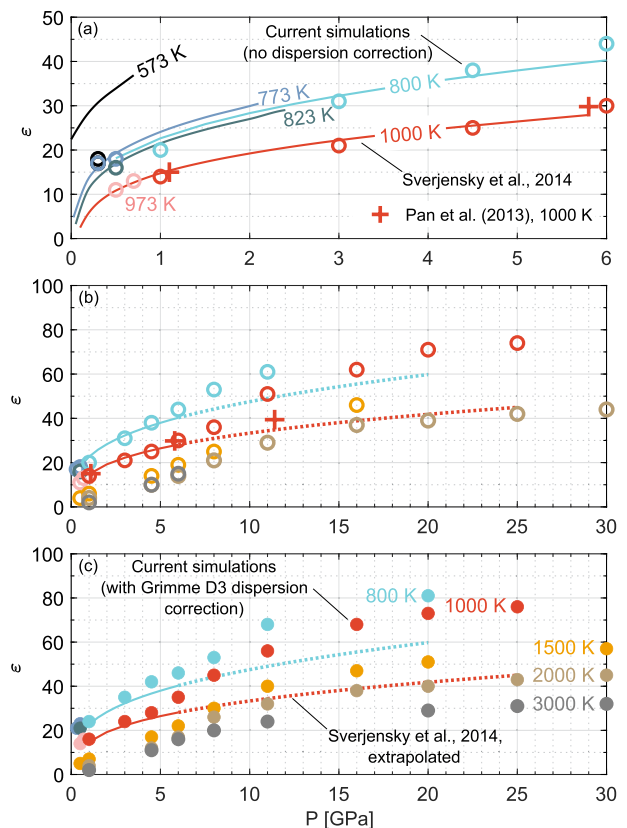

Fig. 2. The dielectric constant of water, ε as a function of P, T. All data are tabulated in Table 1. a) Comparison of ε at ≤6 GPa with results (T contours) based on an empirical equation (Sverjensky et al., 2014) that is valid to 6 GPa. The empirical equation is derived from extrapolation of the Franck et al. (1990) equation, *ab initio* molecular dynamics results at 0.9–1 and 5–5.8 GPa, experimental data from Heger et al. (1980) at 573 to 823 K, and estimates from a literature review (Fernández et al., 1997) at 1000 and 1200 K and Pitzer (1983). The poor correspondence between our calculation and the Sverjensky et al. (2014) result at 0.3 GPa and 573 K is likely because our simulation did not reach equilibrium. Therefore we exclude our 0.3 GPa, 573 K result from further consideration. b, c) Our ε to 30 GPa at selected T for simulations that respectively did not and did include Grimme's D3 dispersion correction. The curves represent the empirical equation of Sverjensky et al., 2014 (from a), dotted where extrapolated.

1073 and 1473 K. Further extrapolation, from 2.5 to 6 GPa, used a linear relationship between $\ln\varepsilon$ and $\ln\rho$ (from the equation of state of Zhang and Duan, 2005). The extrapolation compares well with the 5.8 GPa and 1000 K data point from Pan et al. (2013).

Extrapolating the dielectric constant accurately requires an understanding of the nature of water at deep mantle conditions, but this is currently unclear. For instance, observations of elevated ionic conductivity have led to the suggestion that water is an ionic fluid at extreme P, T (Franck, 1987; French et al., 2010; Huang et al., 2020). Rozsa et al. (2018) have provided further detail based on examination of infrared spectra and results from *ab initio* molecular dynamics simulations at 11 and 20 GPa and 1000 K. According to Rozsa et al. (2018), liquid water dissociates and recombines rapidly, generating short-lived ionic species that act as charge carriers. Associated ionic conductivities are six and seven orders of magnitude larger, respectively, at 11 GPa and 20 GPa than at ambient conditions. Infrared spectra exhibit signatures consistent with the vibrational signatures of hydroxide (OH^{-}) and hydronium (H_3O^{+}) ions. However, the geochemical implications are not yet obvious.

In summary, there are no experimental measurements of ε at >0.5 GPa and >823 K and all extrapolations to higher P, T are based on simple
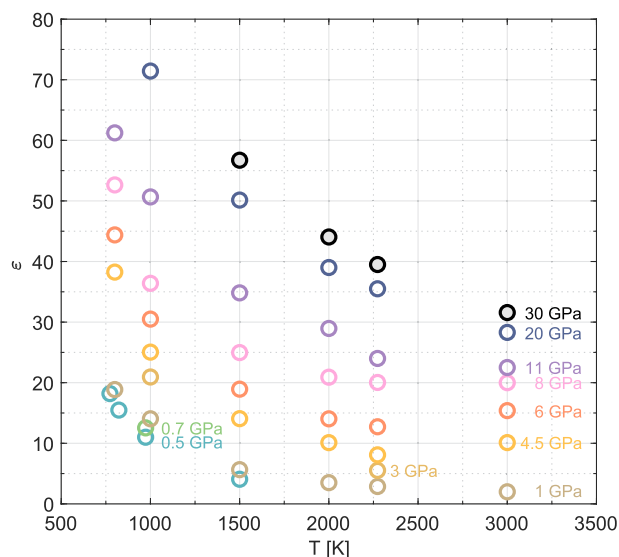
Fig. 3. Variation in ε with T along isobars from 0.3 to 30 GPa.

equations of state. This limits our ability to predict mineral solubilities in many natural geosystems. We have, therefore, used *ab initio* molecular dynamics simulations to provide a grid of density and dielectric constant data for pure water over a P, T range of 0.3–30 GPa and 773–3000 K. We then use the new P–T–ρ–ε values with the HKF equations of state and thermodynamic input parameters (Shock et al., 1992; Facq et al., 2014; Sverjensky et al., 2014; Huang and Sverjensky, 2019) to assess ion complexation and the solubility of carbonates and sulfides under mantle conditions.

2. Computational methods

The static dielectric constant can be determined from a molecular dynamics simulation from fluctuations in the total dipole moment (Eq. (1); Neumann, 1983),

$$\varepsilon = 1 + \frac{\langle \boldsymbol{M}^2 \rangle - \langle \boldsymbol{M} \rangle^2}{3\varepsilon_0 k_B \langle V \rangle T} \tag{1}$$

where ε_0 is the vacuum permittivity, V is the volume of the cubic cell, T is the temperature, k_B is Boltzmann's constant, $\boldsymbol{M}$ is the total dipole moment of the system (i.e., the simulation cell), and the numerator provides the dipole moment variance. The angular brackets denote ensemble averaging.

2.1. Simulations

Simulations are based on density functional theory Born–Oppenheimer molecular dynamics as implemented within the CP2K software package (VandeVondele et al., 2005). CP2K's QUICK-STEP module uses a hybrid Gaussian and plane wave approach for, respectively, linearly expanding molecular orbitals and representing the electronic density (Lippert et al., 1997; Lippert et al., 1999; Vande-Vondele et al., 2005). Our simulations used GTH pseudopotentials (Goedecker et al., 1996; Hartwigsen et al., 1998) to represent core electrons. A molecularly optimized basis set of double-zeta quality represented the valence electrons (VandeVondele and Hutter, 2007). Cutoff and relative density cutoff values related to expansion of the electron density in the Gaussian and plane wave method were 1000 and 60 Ry, respectively. Fowler and Sherman (2020) provide more detail on the convergence testing that led to these inputs.

All simulations used the Perdew–Burke–Ernzerhof (PBE; Perdew et al., 1996) exchange–correlation functional. PBE over-structures water

and overestimates its density at ambient conditions, where dispersion forces and hydrogen bonding exert a strong influence on water structure. However, Fowler and Sherman (2020) found good agreement with data from experiments (Mantegazzi et al., 2013) at elevated P, T in the range 1 GPa < P < 4.5 GPa and 473 K < T < 673 K. Fluid structure is an important consideration in calculating ε because bond length and bond angle can influence the dipole moment. At most P, T points of interest, we ran simulations with and without Grimme's D3 empirical dispersion correction (Grimme et al., 2010) to evaluate the effects of dispersion.

The model system consisted of 110 water molecules in a cubic cell. We defined atomic types and positions prior to beginning each simulation. Simulations used periodic boundary conditions, consistent with dipole moment calculation based on the Berry phase formulation (Resta, 2000; Spaldin, 2012; Kühne et al., 2020). The integration time-step was 0.5 fs. Following initial equilibration, where we discarded at minimum the initial 10 ps of output, most simulations ran for 150–400 ps. Atomic positions relaxed during simulation, leading to a change in average cell volumes compared to input values and in predicted average ρ, compatible with use of the NPT ensemble.

2.2. Solubility calculations

We wrote Python code to evaluate the solvation free energies of aqueous species from the HKF equation of state in conjunction with our functions for $\varepsilon(P, T)$ and $\rho(P, T)$. These routines follow closely those used in SUPCRT92 (Johnson et al., 1992) but without the P, T limitations.

3. Results

Fig. 1 compares our calculated ρ to published ρ for pure water at $\sim$ 1000 K. Table 1 supplies calculated ρ from all simulations and Fig. S1 (supplementary material) plots ρ as a function of P at selected T (800, $\sim$1000, 2000, and 3000 K). Published data in Fig. 1 include results from extrapolation of an equation of state for the density of pure water to 4.5 GPa and 1073 K (Mantegazzi et al., 2013). Aside from one data point at T = 773 K, all Mantegazzi et al. (2013) data in Fig. 1 correspond to T = 973 K. We ran six simulations at three P, T conditions identical to those in the Mantegazzi et al. (2013) dataset: 0.5 GPa, 773 and 973 K and 0.7 GPa, 973 K, with two simulations at each P, T point—one with and one without Grimme's D3 dispersion correction. In addition, we ran a simulation at 1 GPa and 1000 K for comparison with a Mantegazzi et al. (2013) value at 1 GPa and 973 K (Fig. 1). At P $\leq$ 1 GPa, the simulations that did not use a dispersion correction match more closely the Mantegazzi et al. data than simulations that do include a dispersion correction. At higher pressure, the situation is less clear. At 4.5 GPa, the Mantegazzi et al. (2013) data lie between the simulations that respectively do and do not include a dispersion correction. These results may be consistent with evidence (presented below) that hydrogen bonding is minimal at lower P and increases as P rises isothermally. Next, in Fig. 2, we demonstrate the influence of the dispersion correction on ε. Given the generally minor effect of the dispersion correction at mantle conditions, and for ease of comparison with results from Pan et al. (2013), where there is no dispersion correction, we discuss only our uncorrected simulations from here forward. Simulation results that do include the dispersion correction are included in the supplementary material.

Figs. 2 and 3 show our calculated ε values as a function of P and T, respectively, from 0.3 to 30 GPa and 773–3000 K. All results are tabulated in Table 1. The lowest calculated ε, of <10, are at P $\leq$ 1 GPa and elevated T ($\geq$1500 K). The highest ε, near the phase boundary between liquid water and ice VII at 20 GPa and 800 K, is $\sim$80, similar to the ambient-P, T value of 78. Consistent with Helgeson and Kirkham (1974) and Johnson (1987), based on numerical fitting of the Uematsu and Frank (1980) equation to experimental data at P, T of 0.025–0.045 GPa and 623–748 K (Johnson, 1987; Johnson and Norton, 1991), we observe that ε decreases with increasing T at constant P and increases as P rises at constant T. The increase is steeper at lower P. The broad range in ε
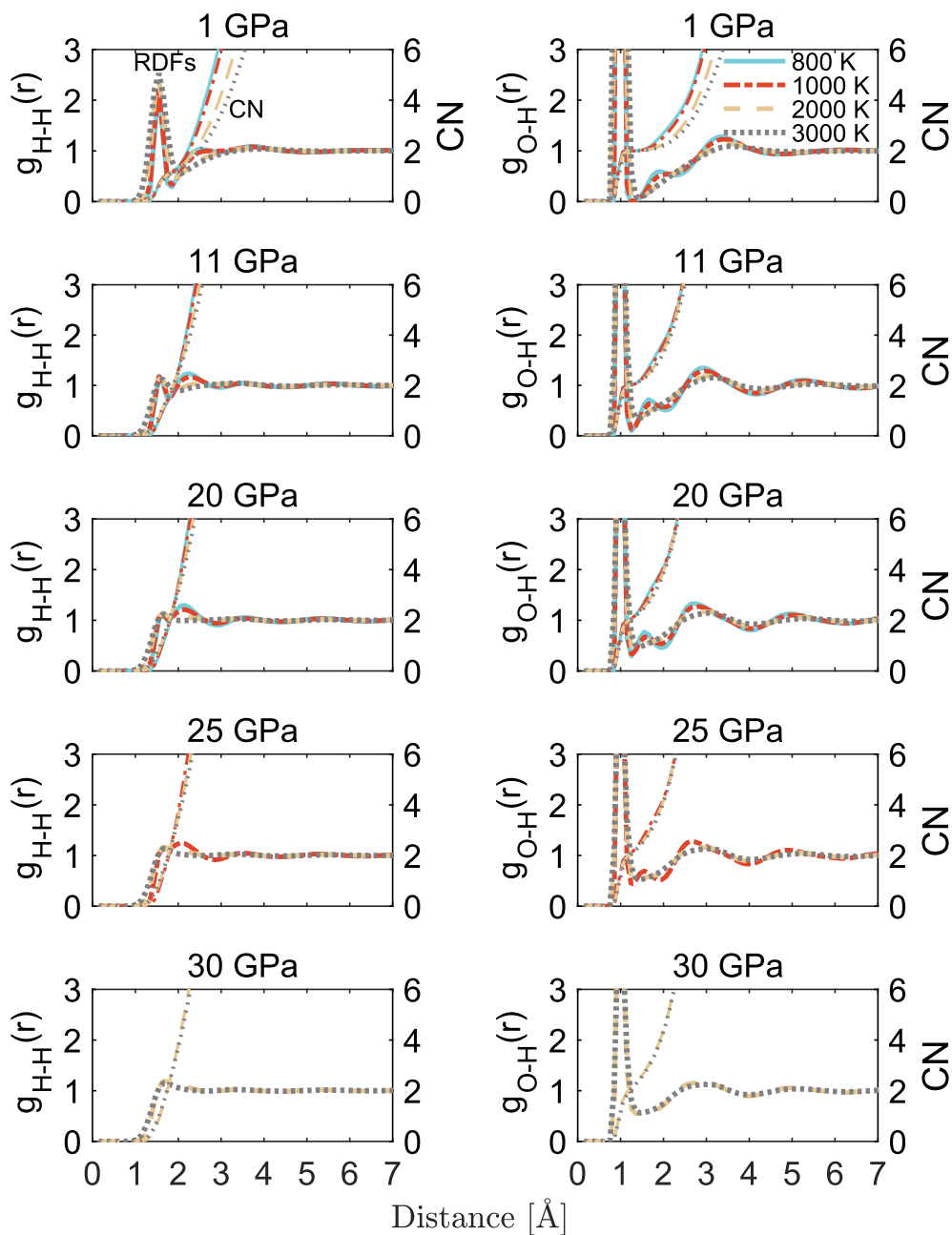
Fig. 4. RDFs ($g_{H-H}(r)$ and $g_{O-H}(r)$; left axis) and coordination numbers (right axis) from our PBE, NPT-ensemble *ab initio* molecular dynamics simulations for pure water at specified P, T. The x axis is interatomic separation, r, in Å. The lowest r values are associated with RDFs of zero, where atoms cannot approach more closely due to their effective widths. All RDFs in this study use a shell size of 0.1 Å.
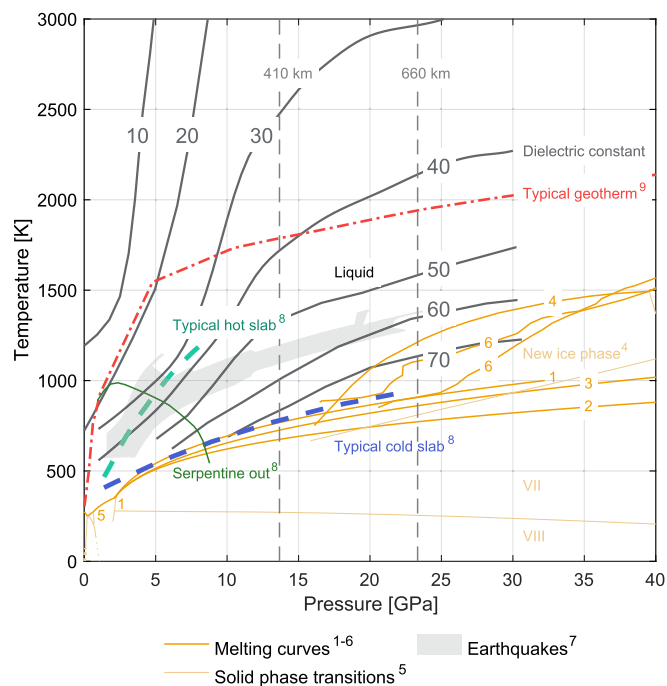
Fig. 5. Contours of ε based on the fit of Eqn. 3 to our simulations overlaid on the water phase diagram, the serpentine-out boundary, a selection of mantle geotherms, and a field defining the P, T loci of deep-focus earthquakes. [1]Lin et al., 2004; [2]Frank et al., 2004; [3]Dubrovinsky and Dubrovinskaia, 2007; [4]Schwager and Boehler, 2008; [5]Journaux et al., 2020; [6]Cheng et al., 2021; [7]Shirey et al., 2021; [8]Ohtani, 2020; [9]Ono, 2008; Ohtani, 2020.

reflects changes in fluid structure as P and T change.

At 0.3–6 GPa and ~1000 K, our ε compare well with those calculated from the empirical equation of Sverjensky et al. (2014) (Fig. 2a). The comparison is reasonably good to T as low as 773 K. There is a significant difference between ε based on the empirical equation and our result at 0.3 GPa and 573 K. This is likely because of slow kinetics that inhibit equilibration in our simulations at low T. There is a linear relationship between ln ρ and ln ε at P <6 GPa, in agreement with Sverjensky et al. (2014). The relationship breaks down at P $\geq$ 6 GPa, likely due to changes in fluid structure (Fig. S2). Figs. 2b, c compare our ε values as a function of pressure at 800 and 1000 K with extrapolations based on Sverjensky et al. (2014). Extrapolation extends from 6 GPa to P close to the liquid water–ice phase boundary. There is a clear difference between our results and the extrapolations. Examples of simulation time versus ε are plotted in Fig. S3.

We and Pan et al. (2013) use system sizes for *ab initio* simulations that are similar (110 and 128 water molecules, respectively) but relatively small compared to typical studies based on classical methods (Fuentes-Azcatl and Alejandre, 2014; Zhang and Sprik, 2016; Afify and Sweatman, 2018; Loche et al., 2021). Pan et al. (2013) compared results from two simple point charge extended (SPC/E) simulations at 1000 K and 0.88 g cm^{-3}, equilibrating 128 water molecules for 20 ps and 1728 water molecules for 1 ns, and found that the calculated dielectric constants differ by <5 %, suggesting that ~100 molecules is sufficient. Pan et al. (2013) reported ε at five P, T state points, 1.1, 5.8, and 11.4 GPa at 1000 K and 5.2 and 8.9 GPa at 2000 K, and focused discussion on the 1000 K simulations, so we ran simulations at 1000 K and 1, 6, and 11 GPa for comparison. Our predicted ε agree well with the Pan et al. (2013) values at ~1 and ~6 GPa (14, and 30 in the current study versus 15 and 29.8, respectively, in Pan et al., 2013) (Fig. 2). Agreement is, however, somewhat poorer at 1000 K and 11 GPa (51 in the current study versus 39.4 in Pan et al., 2013) (Fig. 2). A possible source of discrepancy is that Pan et al. ran simulations of <25 ps in 2013, whereas in 2023, we have been able to run >100 simulations that are each an order of magnitude
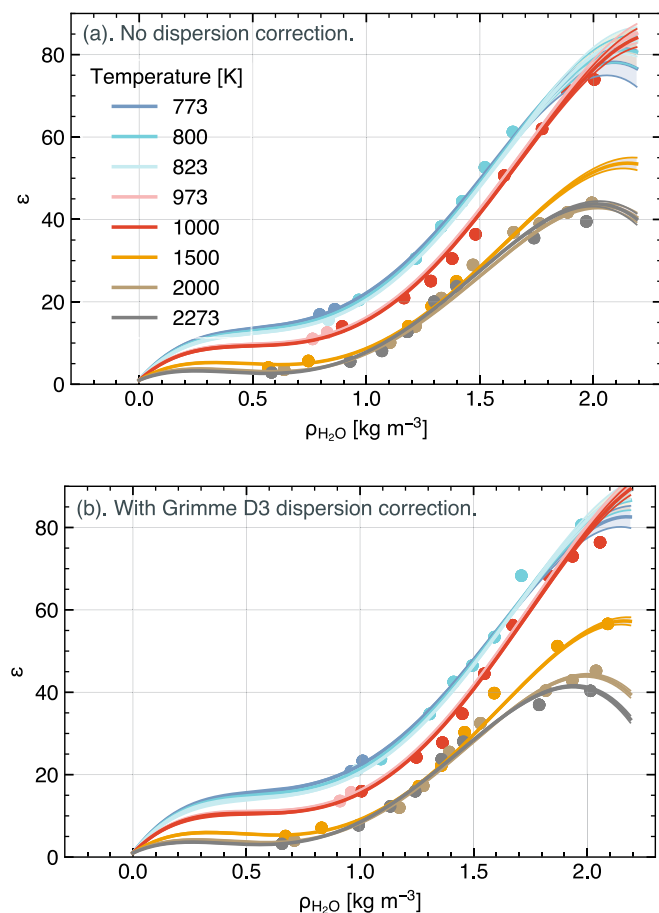

Fig. 6. Equation of state for ε plotted at 773–2273 K (Eq. (3)). a, b) Fit for simulations that do not and do, respectively, use Grimme's D3 dispersion correction. Fit parameters in Table 2. As can be seen in 6a, the highly non-linear nature of the fit means that it should not be extrapolated outside of the density and temperature conditions of the simulations. Covariance matrices in Table S1. Confidence limits are 2 sigma.

Table 2
Coefficients a_i for Eqs. (3) and (4).

Parameter	Fitted value	
	Without Grimme D3	With Grimme D3
a_1	1.824E+2	2.072E+2
a_2	-2.396E+2	-2.371E+2
a_3	-4.518E+1	-5.869E+1
a_4	6.089E-1	1.271E+0
a_5	2.691E+2	2.539E+2
a_6	6.569E+0	9.344E+0
a_7	-1.981E-1	-3.891E-1
a_8	-2.247E+2	-2.475E+2
a_9	7.278E+1	1.002E+2
a_{10}	-2.499E+1	-3.058E+1

longer, even when excluding a minimum of the initial 10 ps of output.

Water structure (e.g., dissociation and hydrogen bonding) is an important consideration when calculating ε. The reaction

$$2H_2O_{(aq)} = H_3O^+_{(aq)} + OH^-_{(aq)} \tag{2}$$

proceeds further to the right at elevated P, T than at ambient conditions (Manning, 2018; Zhang and Duan, 2005). On one hand, we observe that mean square displacement (MSD) diverges for O and H (Fig. S4) with increasing P, T. The implication is that H are increasingly delocalized (i.
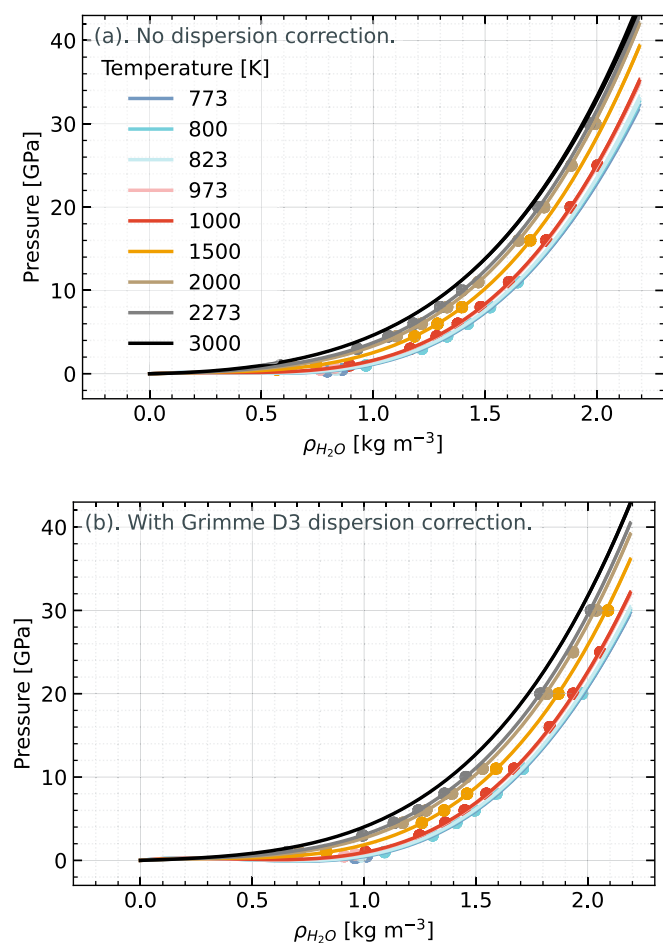
Fig. 7. Equation of state for ρ using the Mie-Grueneisen-Debye formalism, plotted at 773–3000 K. a, b) Fit for simulations that do not and do, respectively, use Grimme's D3 dispersion correction. Fit parameters in Table 3. Covariance matrices in Table S1. Confidence limits are 2 sigma.

Table 3

Mie-Gruneisen-Debye equation of state fit parameters for water: ρ_0, density at reference P, T (10^5 Pa, 773 K); K_0, reference isothermal bulk modulus; K', first derivative of the bulk modulus with respect to pressure; γ_0, reference Gruneisen parameter; q_0, logarithmic volume derivative of the Grüneisen parameter; $\theta_{D,0}$, Debye temperature; χ_ν^2, chi squared. Uncertainties in the parameters can be obtained from the covariance matrices in Table S1.

Parameter	Fitted value	
	Without Grimme D3	With Grimme D3
ρ_0 [kg/m³]	552.5	766.6
K_0 [GPa]	0.211 ± 0.043	0.67 ± 0.45
K'	9.12 ± 1.16	9.53 ± 3.18
γ_0	0.253 ± 0.004	0.298 ± 0.028
q_0	-0.820 ± 0.039	-0.988 ± 0.099
$\theta_{D,0}$ [K]	278	278
χ_ν^2	0.13	0.11

e., not bound to a particular O). Nevertheless, despite the increased mobility of protons, H_2O is the dominant species at all P, T in the current study. We explain this apparent contradiction in terms of increasing fluctuation of H_2O bond angles and bond lengths with increasing P, T after first presenting observations that support the dominance of H_2O.

The first-shell O—H coordination numbers derived from radial distribution functions (RDFs) are ~2 (Fig. 4). Even significant proportions of ionic species may lead to RDF-derived coordination numbers of 2 for water because an RDF-derived coordination number represents a
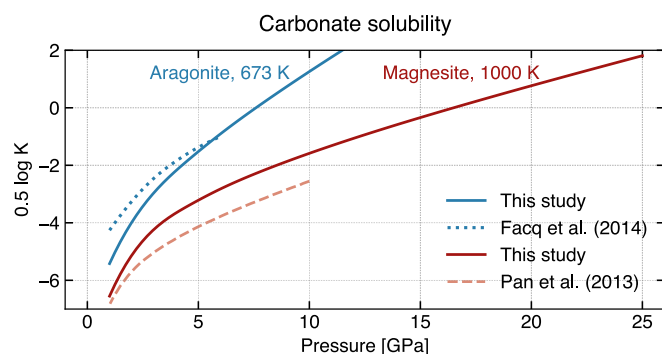

Fig. 8. Comparison of aragonite and magnesite solubility as a function of P with existing predictions. Results from this study are based on new ε and ρ values from *ab initio* molecular dynamics simulations.

simulation average compatible with H_2O alone or equal proportions of H_3O^+ and OH^- (Eqn. 2). However, we observe no structure that reflects distinct O—H bond lengths (Fig. 4), likely if entities other than H_2O were important. Also, visual examination of molecular configurations at selected timesteps demonstrates that H_2O is dominant (Fig. S5). Most significantly, in a simulation of NaCl—H_2O (6 m NaCl) at 20 GPa and 1000 K, Na are solvated by H_2O, not OH^- (Fig. S6), a molecular manifestation of elevated dielectric constant values.

We calculated the relative proportions of H_2O, H_3O^+, and OH^- by enumerating average atomic configurations for each simulation via rings statistics, as implemented in the Rigorous Investigation of Networks Generated using Simulations code (RINGS; Le Roux and Jund, 2010; Le Roux and Jund, 2011), adapted here for application to NPT-ensemble simulations. RINGS accounts for the presence or absence of bonds between two atoms where the atoms are separated by a distance less than that of the corresponding first minimum in the RDF. Our results are consistent with published results. At 1000 and 2000 K, we predict ~1 and 2 mol.%, respectively, of OH^- at $\leq$8 GPa. At 11 GPa and 1000 K, there is ~4.5 mol.% OH^-. At 20 GPa, OH^- is ~6 (1000 K) and 7 (2000 K) mol.%. Fig. S1 in Rozsa et al. (2018) implies 2–3 and ~6–9 mol.% OH^- from their PBE *ab initio* molecular dynamics simulations at (respectively) 11 and 20 GPa and 1000 K. Schwegler et al. (2011) measured an H_3O^+ concentration of ~9.3 mol.% in their PBE *ab initio* molecular dynamics simulation at 30.5 GPa and 1938 K, a concentration that compares reasonably with the ~5.2 mol.% OH^- in our simulation at 2000 K and 30 GPa. From Eqn. 2, the proportions of OH^- and H_3O^+ are identical. However, we use OH^- instead of H_3O^+ to avoid the possibility of confusing H_3O^+ with hydrogen bonded H_2O, which would result in overestimation of the extent of dissociation. Another avenue for potentially overestimating the extent of dissociation is that RDF first minima become less distinct with increasing P, T (Fig. 4).

With regard to hydrogen bonding, the first peak in the intermolecular oxygen–hydrogen RDF ($g_{OH}(r)$), ~1.8 Å at 1 GPa (Fig. 4), exhibits an isobaric decrease in height with increasing T that is consistent with a decrease in the extent of hydrogen bonding. As P increases at constant T, the peak height increases, suggesting that hydrogen bonding increases with increasing P (Koneshan and Rasaiah, 2000; Soper, 2013). The peak also shifts towards the central O as P increases. The presence of hydrogen bonding at P, T well above ambient P, T is consistent with observations from Sahle et al. (2013), who reported hydrogen bonds at P = 0.134 GPa and T as high as 873 K from examination of X-ray Raman spectra and associated *ab initio* molecular dynamics simulations. Rozsa et al. (2018) observed hydrogen bonding at 20 GPa and 1000 K from *ab initio* molecular dynamics simulation results.

Hydrogen bonding can affect ε (Harvey and Friend, 2004; Akizuki et al., 2014). A water molecule that forms fewer hydrogen bonds has a lower average dipole moment. At ambient P, T, the gas phase water monomer dipole moment is ~1.57 times lower than that of a solvated

Table 4

Standard thermodynamic properties and equation of state parameters used in this study in the revised HKF equations of state (Fig. 8). Facq et al. (2014) revised the values for Ca^{2+} and CO_3^{2-}. The parameters for Mg^{2+} are from Shock et al. (1997). Parameters for aragonite and magnesite are from, respectively, Helgeson et al. (1978) and Plummer and Busenberg (1982) and Helgeson et al. (1978). G_f, standard molal Gibbs energy of formation from the elements [cal mol^{-1}]; H_f, standard molal enthalpy of formation from the elements [cal mol^{-1}]; S_r, standard molal entropy [cal mol^{-1} K^{-1}]; V_r, standard molal volume [cm^3 mol^{-1}]. For aqueous species, a1, a2, a3, a4, c1, c2, w_{ref}, and z (species charge) are parameters for the revised HKF equation of state. For the solid species, a, b, and c are coefficients for the heat capacity equation ($C_p = a + bT + cT^{-2}$).

Parameter	Aqueous species		
	Ca^{2+}	Mg^{2+}	CO_3^{2-}
G_f [cal/mol]	-132120.0	-108505.0	-126191.0
H_f [cal/mol]	-129800.0	-111367.0	-161385.0
S_r [cal/mol K]	-13.5	-33.00	-12.95
a_1 [cal/mol bar]	-0.025	-0.08217	0.580
a_2 [cal/mol]	-725	-859.9	500
a_3 [cal K/mol bar]	5.0	8.39	-2
a_4 [cal K/mol]	-24900	-23900.0	-108000
c_1 [cal/mol K]	9.0	20.80	18.000
c_2 [cal K/mol]	-25000.0	-58920.0	-200000
w_{ref} [cal/mol]	124000.0	153720.0	460000.0
z	2.0	2.0	-2.0

Parameter	Solid phase	
	Aragonite, $CaCO_3$	Magnesite, $MgCO_3$
G_f [cal/mol]	-269683.0	-245658.0
H_f [cal/mol]	-288531.0	-265630.0
S_r [cal/mol K]	21.56	15.7
V_r [cm^3/mol]	34.15	28.018
a [cal/mol K]	20.13	19.731
b [cal/mol K^2]	0.01024	0.012539
c [cal K/mol]	-334000.0	-474800.0
T_{max}	600	1000

water molecule in bulk water (Badyal et al., 2000; Coudert et al., 2006; Kemp and Gordon, 2008). As T and molecular kinetic energy increase and ρ decreases towards the critical point (e.g., from 293 to 646 K at the equilibrium vapor P), the average proportion of hydrogen bonds decreases (Hakala et al., 2006; Rastogi et al., 2011; Sahle et al., 2013) and ε decreases from ~78 to 7.22 (Uematsu and Frank, 1980; Fernández et al., 1997). According to Srinivasan and Kay (1977), strengthening of the hydrogen bond network may contribute to positive correlation of neighboring dipoles under isothermal compression. Kang et al. (2011) noted that increasing P, T can broaden the dipole moment distribution, which would increase the dipole moment variance term in Eq. (1) and would lead to larger ε and an increase in intramolecular charge fluctuations.

Fig. 4 also shows the hydrogen–hydrogen ($g_{HH}(r)$) RDF at 1–30 GPa and 800–3000 K. An interesting observation is that first maxima heights decline dramatically with increasing P despite evidence that water dissociation is minimal. Corresponding coordination number profiles exhibit some structure at $r = 1-2$ Å and 1 GPa that reflects the intramolecular proximity of two hydrogen atoms (i.e., as in H_2O), but the structure is not present as P increases. Along with the MSDs, these features are consistent with increasing H—O—H bond angle fluctuation with increasing P, T. The bond angle distribution widens slightly with respect to P increase and significantly with respect to increasing T (Fig. S7). Peak values decline as P and T increase. It is where the bond angle distribution profiles are widest and peaks are lowest that $g_{HH}(r)$ first maxima are lowest, possibly because it is at higher P that hydrogen bonding becomes important, influencing intermolecular interaction, and at higher T that bond angle fluctuation is more vigorous.

According to Rozsa et al. (2018), short-lived ionic species dissociate rapidly and recombine at 11 and 20 GPa and 1000 K. A key point in the current study is that H_2O is the dominant species at all P, T—a large proportion of the liquid water field of the water phase diagram (Fig. 5). There is increasing fluctuation of bond angles and bond lengths with increasing P, T, but it is mostly H_2O that solvates ions.

4. Equations of state for ε and ρ

The dielectric constant can be fitted to a power function in T and ρ (Uematsu and Frank, 1980; Johnson and Norton, 1991),

$$\varepsilon = \sum_{i=0}^{4} k_i(\tau)\widehat{\rho}^i \qquad (3)$$

where $\widehat{\rho}$ is the density of H_2O in g cm^{-3} divided by 1 g cm^{-3} and $\tau = T/T_r$, where T_r is a reference temperature, 298.15 K. This is the functional form used in SUPCRT (Johnson, 1991) for T < 1000 °C and P < 0.5 GPa. We used Eqn. (3) to fit our calculated ε values for H_2O at P, T of 0.3–30 GPa and 773–2273 K (Fig. 6). The $k_i(\tau)$ for i = 1, ..., 4 are calculated from:

$$\begin{aligned}
k_1(\tau) &= a_1\tau^{-1} \\
k_2(\tau) &= a_2\tau^{-1} + a_3 + a_4\tau \\
k_3(\tau) &= a_5\tau^{-1} + a_6\tau + a_7\tau^2 \\
k_4(\tau) &= a_8\tau^{-2} + a_9\tau^{-1} + a_{10}
\end{aligned} \qquad (4)$$

Here, a_1–a_{10} (Table 2) are fitted coefficients for ε. Table S1 provides corresponding covariance matrices.

The parameters were obtained from weighted fits assuming a 1 % error in ε. Uncertainties in the parameters can be obtained from the covariance matrices in Table S1.

We fitted the densities from our NPT simulations with the Mie-Gruneisen-Debeye thermal equation of state as implemented in the Burnman library (Myhill et al., 2023) (Fig. 7). The base isotherm was 773 K, defined from the third-order Birch-Murnaghan finite-strain static equation of state. Fit parameters appear in Table 3. The covariance matrices are in Table S1 (supplementary data). We do not recommend extrapolating the fits outside the ranges provided here (0.3 to 30 GPa and 773–3000 K).

5. Application of modified HKF equations to aqueous speciation and mineral solubility from the crust to the deep mantle

Our *ab initio* simulations show that ε varies dramatically in the mantle, from < 10 at P ≤ 1 GPa and T ≥ 1500 K, similar to ε associated with the liquid–vapor critical point (~6), to values approaching those at ambient conditions (~80) close to the water–ice phase boundary at transition zone (20 GPa) and lower mantle (25 GPa) P (Fig. 5). At lower crustal and upper mantle conditions, $\varepsilon \geq 40$ coincides with shallower and colder (<1 GPa and 600 K) slab tops (Fig. 5). In the deep mantle, along an average geotherm (e.g., 20 GPa, 2000 K; 30 GPa, 2000 and 2273 K), ε is ≥ 40 (Fig. 5). These results suggest that water is highly reactive in a large part of the mantle.

The HKF EOS extrapolates the Born model of solvation (Born, 1920) to account for the P, T dependence of ε. Given the P and T derivatives of ε (evaluated here from Eq. (4)):

$$Y = \frac{1}{\varepsilon^2}\left(\frac{\partial \varepsilon}{\partial T}\right)_P ; X = \left(\frac{\partial Y}{\partial T}\right)_P ; Q = \frac{1}{\varepsilon^2}\left(\frac{\partial \varepsilon}{\partial P}\right)_T \qquad (5)$$

the standard partial molar volumes and heat capacities of an ion are parameterized as (Tanger and Helgeson, 1988):

$$\Delta \overline{V}_{s,j}^o = a_1 + \frac{a_2}{\psi + P} + \left(a_3 + \frac{a_4}{(\psi + P)}\right)\left(\frac{1}{T - \theta}\right) - \omega Q + \left(\frac{1}{\varepsilon} - 1\right)\left(\frac{\partial \omega_j}{\partial P}\right)_T \qquad (6)$$

$$\Delta \overline{C}_{p_{s,j}}^{o} = c_1 + \frac{c_2}{(T-\theta)^2} - \frac{2T}{(T-\theta)^3}\left[a_3(P-P_r)+a_4 ln\left(\frac{\psi+P}{\psi+P_r}\right)\right] + \omega_j TX$$
$$+ 2TY\left(\frac{\partial \omega_j}{\partial T}\right)_P - T\left(\frac{1}{\varepsilon}-1\right)\left(\frac{\partial^2 \omega_j}{\partial T^2}\right)_P \tag{7}$$

Here, ψ and θ are solvent parameters (equal to 2600 bars and 228 K, respectively), while a_1, a_2, a_3, a_4 and $c_1, c_2,$ are P- and T-independent parameters characteristic of the aqueous ion or electrolyte. The final parameter characteristic of each ion is the P and T-dependent Born coefficient, ω_j, modelled by Tanger and Helgeson (1988) as

$$\omega_j = \eta\left(\frac{Z^2}{(r_{e,P_r,T_r}+|Z|g)} - \frac{Z}{(3.082+g)}\right) \tag{7}$$

Here, η is a constant (1.66027E + 5 Å•cal/mol), Z is charge, g is a function of T and solvent density (Shock et al., 1992), and r_{e,P_r,T_r} is the effective electrostatic radius at reference P, T ($P_r = 1$ bar; T_r=298.15 K):

$$r_{e,P_r,T_r} = \frac{Z^2}{(\omega_{ref}/\eta+Z/3.082)} \tag{8}$$

where ω_{ref} is the Born coefficient at P_r, T_r.

Tanger and Helgeson (1988) used experimental data for aqueous electrolytes (partial molal volumes, compressibilities, and isobaric heat capacities) to infer the standard partial molal properties of associated aqueous ions. They regressed the parameters in the semi-empirical expressions for the nonsolvation contributions for electrolytes (parameters a_1, a_2, a_3, a_4 and $c_1, c_2,$ in the HKF model). From the resulting parameters for electrolytes, using the additivity principle and the convention that all properties of the H$^+$ ion are zero at any P, T, Tanger and Helgeson (1988) estimated HKF parameters of several aqueous ions and complexes. These form the HKF dataset, later used to derive HKF parameters for other ions and complexes. Subsequent parameters for individual species are obtained from experimental data or systematic correlations between volumes ($\overline{V}^0$), heat capacities ($\overline{C}_P^0$) and the seven empirical equation of state coefficients $a_1, a_2, a_3, a_4, c_1, c_2,$ and ω for each ion of

interest (e.g., Shock and Helgeson, 1988; Shock et al., 1992; Shock et al., 1997).

Below we use our calculated $\varepsilon(P, T)$ along with the HKF equations of state (Helgeson et al., 1981; Tanger and Helgeson, 1988) and ion parameters from existing literature (Shock et al., 1992; Sverjensky et al., 2014) to evaluate the reactivity of aqueous mantle fluids. In particular, we calculate the solubilities of carbonates and sulfides and the stability of metal complexes.

5.1. Magnesite and aragonite solubilities at extreme pressures

The solubility of carbonate minerals can be represented as

$$\text{MCO}_3(\text{s}) = \text{M}^{2+} + \text{CO}_3^{2-} \tag{9}$$

where M represents Ca, Mg, Ca$_{0.5}$Mg$_{0.5}$, or Fe, and s denotes the solid state. The quantity 0.5 log K (where K is the equilibrium constant for the reaction) represents the minimum solubility because it neglects the formation of HCO$_3^-$, H$_2$CO$_3^0$, and various ion pairs such as MgCO$_3^0$, Mg(OH)$^+$, etc. (Huang and Sverjensky, 2019). Pan et al (2013) calculated the solubility of carbonate minerals (calcite, aragonite, dolomite, magnesite, and siderite) at upper mantle conditions (1–11 GPa at 1000 K) using the HKF equation of state and their ρ and ε calculated at 1.1, 5.8, and 11.4 GPa. Note that the HKF parameters used by Pan et al (2013) for P of 5.8 and 11.4 GPa appear to be derived from a study of carbonate speciation up to a P of 6 GPa (Facq et al., 2014) (Fig. 8). These high-P HKF parameters reflect a change in the speciation of the CO$_3^{2-}$ ion in water—from CO$_2$ and H$_2$O at lower P to H$_2$CO$_3$ at higher P, as discussed by Facq et al. (2014) for M^{2+} and CO$_3^{2-}$ solvation free energies. Pan et al. (2013) find, at 1000 K, 0.5 log K = –6.8 at 1 GPa and 0.5 log K = –2.6 at 11 GPa, implying that P increase enhances the solubility of magnesite. We have recalculated the free energies for magnesite and aragonite dissolution at high P using our values for ρ and ε up to 25 GPa. We used the standard Gibbs free energies for solid phases based on Helgeson et al. (1978), where mineral volume is independent of P and T. Equation of state parameters for the solid phases are from the slop98 parameter set (Table 4; GEOPIG, 2010). Data for aragonite and magnesite are valid to a maximum T of 600 and 1000 K, respectively. We

Table 5

Standard thermodynamic properties and equation of state parameters of solid and aqueous species. Parameters for Cu$^+$, HS$^-$, and Cl$^-$ are from Shock et al. (1997). Parameters for Fe^{2+} are from Shock and Helgeson (1988), Helgeson (1985), Shock and Helgeson (1989) and Shock et al. (1997). For CuCl$_2^-$ and FeCl$_2^0$, parameters are from Sverjensky et al. (1997). Chalcopyrite parameters are from Helgeson et al. (1978) and Pankratz and King (1970). Further detail in Table 4.

Parameter	Aqueous species					
	Cu$^+$	Fe^{2+}	HS$^-$	Cl$^-$	CuCl$_2^-$	FeCl$_2^0$
ΔG_f^0 [cal/mol]	11950.0	-21870.0	2860.0	-31379.0	-58038.0	-73480.0
ΔH_f^0 [cal/mol]	17132.0	-22050.0	-3850.0	-39933.0	-72903.0	-78490.0
S_r [cal/mol K]	9.7	-25.3	16.3	13.56	26.96	43.0
a_1 [cal/mol bar]	0.0807	-0.07867	0.50119	0.4032	0.83943	0.55057
a_2 [cal/mol]	-580.4	-969.69	497.99	480.1	1271.82	566.5
a_3 [cal K/mol bar]	8.0165	9.5479	3.4765	5.563	0.7442	3.5164
a_4 [cal K/mol]	-25390.0	-23780.0	-29849.0	-28470.0	-33047.0	-30131.0
c_1 [cal/mol K]	17.9233	14.786	3.42	-4.4	36.7555	22.9295
c_2 [cal K/mol]	-2438.0	-46437.0	-62700.0	-57140.0	36846.0	29135.0
w_{ref} [cal/mol]	40460.0	143820.0	144100.0	145600.0	122190.0	-3800.0
z	1.0	2.0	-1.0	-1.0	-1.0	0.0

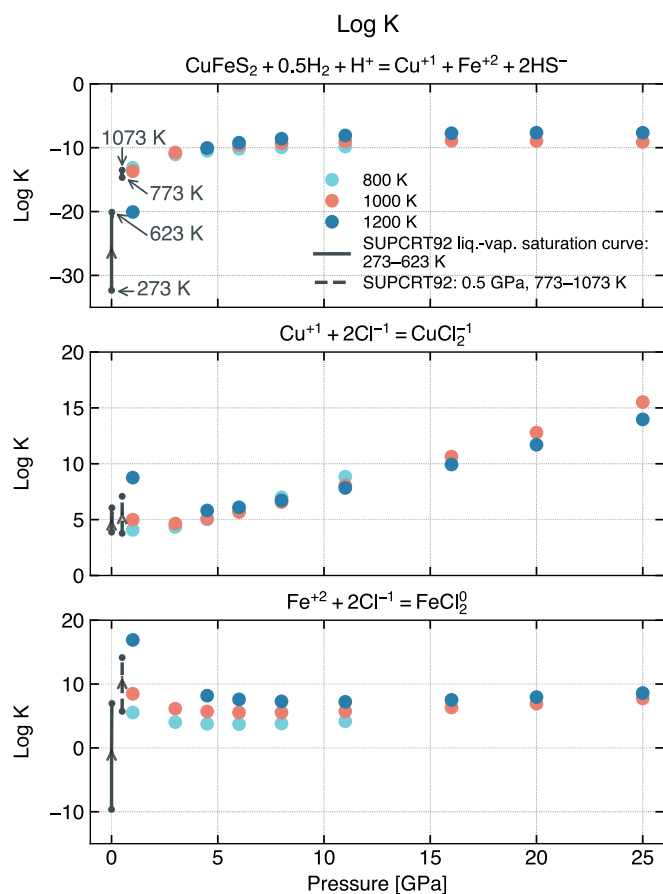|	Solid species					
	Chalcopyrite, CuFeS$_2$					
G_f [cal/mol]	-44900.0					
H_f [cal/mol]	-44453.0					
S_r [cal/mol K]	31.15					
V_r [cm^3/mol]	42.83					
a [cal/mol K]	41.22					
b [cal/mol K^2]	0.0					
c [cal K/mol]	0.0					
T_{max}	1200.0					

Fig. 9. A) Log k of chalcopyrite at mantle conditions calculated from the HKF equations of state for a hydrothermal fluid with pH = 4 and f_{H_2} of 91 (Hunt and Lamb, 2019). The calculation used ρ and ε from this study. Subvertical curves show log K along the liquid–vapor curve and under supercritical conditions up to 0.5 GPa (i.e., at low-P, T) calculated using SUPCRT92 (Johnson et al., 1992). A key point is that log K increases with increasing P so that chalcopyrite solubility is higher than in low-P, T crustal ore-forming fluids (a) even in the absence of Cl^- complexation reactions (b, c).

also used the HKF parameters from Facq et al. (2014) at high P (Table 4). With regard to the HKF equation of state parameters for dissolved species, we observed that slop98 inputs generate results that correspond closely with solubilities from Pan et al. (2013) at 1 GPa.

From our parameterizations for ρ and ε, along with the HKF parameters described above, we calculate solubilities that are somewhat higher than those calculated by Pan et al. (2013) (Fig. 8). Our results support the conclusion of Pan et al (2013) that the dielectric constant of water under mantle conditions is high enough to yield high aqueous solubilities for carbonate phases in the mantle. It is conceptually convenient to relate log K to the molal solubility of carbonates. This is certainly true for very dilute solutions. Indeed, we find that the solubility increases with P such that in regions with high fluid contents (e.g., in the mantle immediately above subducting slabs), carbonates may be stripped from the mantle. In the absence of an activity-composition model, however, we don't know the physical consequence of the extremely large log Ks we have calculated for carbonate. We tentatively speculate that carbonates in aqueous fluids would form a hydrous carbonate melt under mantle conditions. However, a great deal of molecular science needs to be done to relate activities to molal concentrations under these conditions.

5.2. Metal complexation and chalcopyrite solubility

Within ore-forming hydrothermal systems, disseminated sulfides are

dissolved by fluids containing complexing ligands such as H_2O, Cl^-, and HS^-. The dissolution of chalcopyrite ($CuFeS_2$) depends on pH and hydrogen fugacity:

$$CuFeS_2 + \frac{1}{2}H_2 + H^+ = Cu^+ + Fe^{2+} + 2HS^- \qquad (10)$$
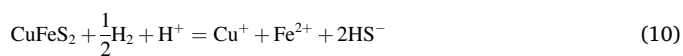
We evaluated log K for the reaction above. Thermodynamic data for chalcopyrite are defined up to 1200 K (Table 5; GEOPIG, 2010). Therefore, 1200 K is the upper T limit of our calculations. This is approximately consistent with slab top T in the deep mantle (Holt and Condit, 2021).

Fig. 9 shows our log K predictions under mantle conditions. Also shown are log K for low P, T conditions associated with ore-forming fluids in the crust (i.e., along the liquid–vapor curve and under supercritical conditions up to 0.5 GPa) calculated using SUPCRT92 (Johnson et al., 1992). With increasing P, log K increases to yield a high solubility for chalcopyrite even in the absence (Fig. 9a) of Cl^- complexation reactions (Fig. 9b, c). The solubility of chalcopyrite under mantle conditions is higher than that found in crustal ore-forming fluids.

In crustal fluids, the solubility of metal sulfides is enhanced by the complexation of metals by Cl^- ions in hydrothermal fluids. These complexation reactions are enhanced with T due to the decrease in the dielectric constant of water. We evaluated the effect of P on complexation reactions under mantle conditions (Fig. 9b, c). As P rises, coinciding with the bulk of the upper mantle, most log K values for complexation reactions involving Cl^- fall below those in typical crustal ore-forming systems, as represented by the near-vertical curves in Fig. 9. Increasing P can therefore decrease the stability of Fe and Cu complexes in the shallow mantle (due to the increase in the dielectric constant), but not enough to overcome the effect of T. Hence, metal complexation in the upper mantle should enhance metal sulfide solubility, as in crustal fluids. At higher P, through the transition zone and into the lower mantle, complexation increases. Log K values can rise above those in typical crustal ore-forming systems (Fig. 9b). The associated change in ε is relatively small (Fig. 5), so the increase reflects the negative molar volume change of complexation at high P. The negative reaction volumes are linked with the a2–a4 values from Table 5. Whether the values are accurate at the extreme P explored here is uncertain.

The main finding is that deep mantle ($\sim$>10 GPa, 1000 K) fluids can potentially dissolve primary sulfides and transport metals even more efficiently than can crustal fluids associated with ore genesis in porphyry copper deposits. This suggests that exsolved fluids from subducted slabs scavenge metals from the slab and overlying mantle wedge. The metals in porphyry copper deposits might have a very deep origin.

6. Conclusions

We report ε and ρ of pure water at deep mantle P, T conditions based on results of CP2K NPT *ab initio* molecular dynamics simulations. These results significantly extend our knowledge of ε from previous studies and support the concept that water is a highly reactive solvent in the deep mantle.

Our new parameterizations of ε and ρ lead to solubilities for aragonite and magnesite that are somewhat higher compared to Pan et al (2013) and to results from the related DEW model (Sverjensky et al., 2014). We calculated the solubility of chalcopyrite at a specified f_{H_2} and pH and Cl complexation of Cu and Fe, finding that deep fluids ($\sim$>10 GPa) have an even greater capacity to dissolve sulfide minerals and transport metals than crustal fluids linked with the formation of porphyry copper deposits. Fluids associated with subducted slabs may therefore scavenge metals efficiently from the slab and the overlying mantle wedge, potentially leading to a deep origin for porphyry copper deposit metals.

Data availability

Data are available through the British Geological Survey's National Geoscience Data Center at https://doi.org/10.5285/b435d6b4-3628-43cc-aa24-6175ed5eef16.

CRediT authorship contribution statement

Sarah J. Fowler: Writing – review & editing, Writing – original draft, Investigation, Funding acquisition, Conceptualization. **David M. Sherman:** Writing – review & editing, Writing – original draft, Investigation. **John P. Brodholt:** Writing – review & editing, Writing – original draft, Investigation, Funding acquisition. **Oliver T. Lord:** Writing – review & editing, Writing – original draft, Investigation, Funding acquisition.

Declaration of competing interest

The authors declare that they have no known competing financial interests or personal relationships that could have appeared to influence the work reported in this paper.

Appendix A. Supplementary material

Supplementary material to this article can be found online at https://doi.org/10.1016/j.gca.2024.03.012.

References

Afify, N.D., Sweatman, M.B., 2018. Classical molecular dynamics simulation of microwave heating of liquids: the case of water. J. Chem. Phys. 148, 024508.

Akizuki, M., Fujii, T., Hayashi, R., Oshima, Y., 2014. Effects of water on reactions for waste treatment, organic synthesis, and bio-refinery in sub- and supercritical water. J. Biosci. Bioeng. 117, 10–18.

Badyal, Y.S., Saboungi, M.-L., Price, D.L., Shastri, S.D., Haeffner, D.R., Soper, A.K., 2000. Electron distribution in water. J. Chem. Phys. 112, 9206–9208.

Born, M., 1920. Volumen und hydratationswärme der Ionen. Z. Phys. 1, 45–48.

Bovay, T., Rubatto, D., Lanari, P., 2021. Pervasive fluid-rock interaction in subducted oceanic crust revealed by oxygen isotope zoning in garnet. Contrib. Mineral. Petrol. 176, 55.

Chaplin, M.F., 2007. Water's hydrogen bond strength. arXiv: Soft Condensed Matter 87–104.

Chen, B., Ivanov, I., Klein, M.L., Parrinello, M., 2003. Hydrogen bonding in water. Phys. Rev. Lett. 91, 215503.

Cheng, B., Bethkenhagen, M., Pickard, C.J., Hamel, S., 2021. Phase behaviours of superionic water at planetary conditions. Nat. Phys. 17, 1228–1232.

Coudert, F.-X., Vuilleumier, R., Boutin, A., 2006. Dipole moment, hydrogen bonding and IR spectrum of confined water. ChemPhysChem 7, 2464–2467.

Das, S., Basu, A.R., Mukherjee, B.K., 2017. In situ peridotitic diamond in Indus ophiolite sourced from hydrocarbon fluids in the mantle transition zone. Geology 45, 755–758.

Drewitt, J.W.E., Walter, M.J., Brodholt, J.P., Muir, J.M.R., Lord, O.T., 2022. Hydrous silicate melts and the deep mantle H_2O cycle. Earth Planet. Sci. Lett. 581, 117408.

Dubrovinsky, L., Dubrovinskaia, N., 2007. Melting of ice VII and new high-pressure, high-temperature amorphous ice. In: Ohtani, E. (Ed.). Advances in High-Pressure Mineralogy, 421, doi: 10.1130/2007.2421(07).

Faccenda, M., 2014. Water in the slab: a trilogy. Tectonophysics 614, 1–30.

Facq, S., Daniel, I., Montagnac, G., Cardon, H., Sverjensky, D., 2014. *In situ* Raman study and thermodynamic model of aqueous carbonate speciation in equilibrium with aragonite under subduction zone conditions. Geochim. Cosmochim. Acta 132, 375–390.

Faulkner, D.R., Rutter, E.H., 2001. Can the maintenance of overpressured fluids in large strike-slip fault zones explain their apparent weakness? Geology 29, 503–506.

Fernández, D.P., Mulev, Y., Goodwin, A.R.H., Levelt Sengers, J.M.H., 1995. A database for the static dielectric constant of water and steam. J. Phys. Chem. Ref. Data 24, 33–70.

Fernández, D.P., Goodwin, A.R.H., Lemmon, E.W., Levelt Sengers, J.M.H., Williams, R.C., 1997. A formulation for the static permittivity of water and steam at temperatures from 238 K to 873 K at pressures up to 1200 MPa, including derivatives and Debye-Hückel coefficients. J. Phys. Chem. Ref. Data. 26, 1125–1166.

Fowler, S.J., Sherman, D.M., 2020. The nature of NaCl-H_2O deep fluids from ab initio molecular dynamics at 0.5-4.5 GPa, 20–800°C, and 1–14 m NaCl. Geochim. Cosmochim. Acta 277, 243–264.

Franck, E.U., 1987. Fluids at high pressures and temperatures. Pure Appl. Chem. 59, 25–34.

Franck, E.U., Rosenzweig, S., Christoforakos, M., 1990. Calculation of the dielectric-constant of water to 1000°C and very high pressures. Ber. Bunsenges. Phys. Chem. 94, 199–203.

Frank, M.R., Fei, Y., Hu, J., 2004. Constraining the equation of state of fluid H_2O to 80 GPa using the melting curve, bulk modulus and thermal expansivity of Ice VII. Geochim. Cosmochim. Acta 68, 2781–2790.

French, M., Mattsson, T.R., Redmer, R., 2010. Diffusion and electrical conductivity in water at ultrahigh pressures. Phys. Rev. B 82, 174108.

Fuentes-Azcatl, R., Alejandre, J., 2014. Non-polarizable force field of water based on the dielectric constant: TIP4P/ε. J. Phys. Chem. B 118 (5), 1263–1272.

GEOPIG, 2010. Numerical Tools. http://geopig.asu.edu/?q=tools. Retrieved 28 September, 2022.

Goedecker, S., Teter, M., Hutter, J., 1996. Separable dual-space Gaussian pseudopotentials. Phys. Rev. B 54, 1703–1710.

Grimme, S., Antony, J., Ehrlich, S., Krieg, H., 2010. A consistent and accurate ab initio parametrization of density functional dispersion correction (DFT-D) for the 94 elements H-Pu. J. Chem. Phys. 132, 154104-1–154104-19.

Gu, T., Pamato, M.G., Novella, D., Alvaro, M., Fournelle, J., Brenker, F.E., Wang, W., Nestola, F., 2022. Hydrous peridotitic fragments of Earth's mantle 660 km discontinuity sampled by a diamond. Nat. Geosci. 950–954.

Hakala, M., Nygård, K., Manninen, S., Huotari, S., Buslaps, T., Nilsson, A., Pettersson, L.G., Hämäläinen, K., 2006. Correlation of hydrogen bond lengths and angles in liquid water based on Compton scattering. J. Chem. Phys. 125, 084504.

Hartwigsen, C., Goedecker, S., Hutter, J., 1998. Relativistic separable dual-space Gaussian pseudopotentials from H to Rn. Phys. Rev. B 58, 3641–3662.

Harvey, A.H., Friend, D.G., 2004. Physical properties of water. In: Palmer, D.A., Fernández–Prini, R., Harvey, A.H. (Eds.), Aqueous Systems at Elevated Temperatures and Pressures: Physical Chemistry in Water, Steam and Hydrothermal Solutions. Elsevier Academic Press, pp. 1–27.

Heger, K., Uematsu, M., Franck, E.U., 1980. The static dielectric constant of water at high pressures and temperatures to 500 MPa and 550°C. Berichte Der Bunsen-Gesellschaft 84, 758–762.

Helgeson, H.C., 1985. Errata II. Thermodynamics of minerals, reactions, and aqueous solutions at high pressures and temperatures. Am. J. Sci. 285, 845–855.

Helgeson, H.C., Delany, J.M., Nesbitt, H.W., Bird, D.K., 1978. Summary and critique of the thermodynamic properties of rock-forming minerals. Am. J. Sci. 278-A, 1–229.

Helgeson, H.C., Kirkham, D.H., 1974. Theoretical prediction of the thermodynamic behavior of aqueous electrolytes at high pressures and temperatures; I, Summary of the thermodynamic/electrostatic properties of the solvent. Am. J. Sci. 274, 1089–1198.

Helgeson, H.C., Kirkham, D.H., Flowers, D.C., 1981. Theoretical prediction of the thermodynamic behavior of aqueous electrolytes at high pressures and temperatures: IV. Calculation of activity coefficients, osmotic coefficients, and apparent molal and standard and relative partial molal properties to 600°C and 5 kb. Am. J. Sci. 281, 1249–1516.

Hickman, S., Sibson, R.H., Bruhn, R., 1995. Introduction to special section: mechanical involvement of fluids in faulting. J. Geophys. Res. 100, 12831–12840.

Hirschmann, M.M., 2006. Water, melting and the deep earth H_2O cycle. Annu. Rev. Earth Planet. Sci. 34, 629–653.

Holt, A.F., Condit, C.B., 2021. Slab temperature evolution over the lifetime of a subduction zone. Geochem. Geophys. Geosyst. 22, e2020GC009476.

Huang, P., Liu, H., Lv, J., Li, Q., Long, C., Wang, Y., Chen, C., Hemley, R.J., Ma, Y., 2020. Stability of H_3O at extreme conditions and implications for the magnetic fields of Uranus and Neptune. Proc. Nat. Acad. Sci. 117, 5638–5643.

Huang, F., Sverjensky, D.A., 2019. Extended Deep Earth water model for predicting major element mantle metasomatism. Geochim. Cosmochim. Acta 254, 192–230.

Hunt, L.E., Lamb, W.M., 2019. Application of mineral equilibria to estimate fugacities of H_2O, H_2, and O_2 in mantle xenoliths from the southwestern U.S.A. Am. Min. 104, 333–347.

Irwin, W.P., Barnes, I., 1975. Effect of geologic structure and metamorphic fluids on seismic behavior of the San Andreas Fault System in central and northern California. Geology 3, 713–716.

Johnson, J.W., Norton, D., 1991. Critical phenomena in hydrothermal systems: state, thermodynamic, electrostatic, and transport properties of H_2O in the critical region. Am. J. Sci. 291, 541–648.

Johnson, J.W., Oelkers, E.H., Helgeson, H.C., 1992. SUPCRT92: a software package for calculating the standard molal thermodynamic properties of minerals, gases, aqueous species, and reactions from 1 to 5000 bars and 0 to 1000 °C. Comput. Geosci. 18, 899–947.

Johnson, J.W., 1987. Critical phenomena in hydrothermal systems: state, thermodynamic, transport, and electrostatic properties of in the critical region. Doctoral dissertation, The University of Arizona.

Journaux, B., Brown, J.M., Pakhomova, A., Collings, I.E., Petitgirard, S., Espinoza, P., Boffa Ballaran, T., Vance, S.D., Ott, J., Cova, F., Garbarino, G., Hanfland, M., 2020. Holistic approach for studying planetary hydrospheres: Gibbs representation of ices thermodynamics, elasticity, and the water phase diagram to 2,300 MPa. J. Geophys. Res. Planets 125, e2019JE006176.

Kang, D., Dai, J., Yuan, J., 2011. Changes of structure and dipole moment of water with temperature and pressure: a first principles study. J. Chem. Phys. 135, 024505.

Karato, S., 2011. Water distribution across the mantle transition zone and its implications for global material circulation. Earth Planet. Sci. Lett. 301, 413–423.

Karato, S., Karki, B., Park, J., 2020. Deep mantle melting, global water circulation and its implications for the stability of the ocean mass. Prog. Earth Planet. Sci. 7, 76.

Kemp, D.D., Gordon, M.S., 2008. An interpretation of the enhancement of the water dipole moment due to the presence of other water molecules. Phys. Chem. A 112, 4885–4894.

Khan, A., Shankland, T.J., 2012. A geophysical perspective on mantle water content and melting: inverting electromagnetic sounding data using laboratory-based electrical conductivity profiles. Earth Planet. Sci. Lett. 317–318, 27–43.

Kirby, S.H., Wang, K., Brocher, T.M., 2014. A large mantle water source for the northern San Andreas fault system: a ghost of subduction past. Earth Planet. Sp. 66, 67.

Koneshan, S., Rasaiah, J.C., 2000. Computer simulation studies of aqueous sodium chloride solutions at 298 K and 683 K. J. Chem. Phys. 113, 8125–8137.

Kühne, T.D., Iannuzzi, M., Del Ben, M., Rybkin, V.V., Seewald, P., Stein, F., Laino, T., Khaliullin, R.Z., Schütt, O., Schiffmann, F., Golze, D., Wilhelm, J., Chulkov, S., Bani-Hashemian, M.H., Weber, V., Borštnik, U., Taillefumier, M., Jakobovits, A.S., Lazzaro, A., Pabst, H., Müller, T., Schade, R., Guidon, M., Andermatt, S., Holmberg, N., Schenter, G.K., Hehn, A., Bussy, A., Belleflamme, F., Tabacchi, G., Glöß, A., Lass, M., Bethune, I., Mundy, C.J., Plessl, C., Watkins, M., VandeVondele, J., Krack, M., Hutter, J., 2020. CP2K: an electronic structure and molecular dynamics software package - Quickstep: efficient and accurate electronic structure calculations. J. Chem. Phys. 152, 194103.

Le Roux, S., Jund, P., 2011. Erratum: Ring statistics analysis of topological networks: new approach and application to amorphous GeS$_2$ and SiO$_2$ systems. [Comput. Mater. Sci. 49, 2010, 70-83]. Comp. Mater. Sci. 50, 1217, doi: 10.1016/j.commatsci.2010.10.012.

Le Roux, S., Jund, P., 2010. Ring statistics analysis of topological networks: new approach and application to amorphous GeS$_2$ and SiO$_2$ systems. Comp. Mater. Sci. 49, 70–83.

Li, J., Wang, X., Wang, X., Yuen, D.A., 2013. P and SH velocity structure in the upper mantle beneath Northeast China: evidence for a stagnant slab in hydrous mantle transition zone. Earth Planet. Sci. Lett. 367, 71–81.

Lin, Y., Hu, Q., Meng, Y., Walter, M., Mao, H.-K., 2020. Evidence for the stability of ultrahydrous stishovite in Earth's lower mantle. Proc. Nat. Acad. Sci. 117, 184–189.

Lin, J.-F., Militzer, B., Struzhkin, V.V., Gregoryanz, E., Hemley, R.J., Mao, H.-K., 2004. High pressure-temperature Raman measurements of H$_2$O melting to 22 GPa and 900 K. J. Chem. Phys. 121, 8423–8427.

Lippert, G., Hutter, J., Parrinello, M., 1997. A hybrid Gaussian and plane wave density functional scheme. Mol. Phys. 92, 477–488.

Lippert, G., Hutter, J., Parrinello, M., 1999. The Gaussian and augmented-plane-wave density functional method for ab initio molecular dynamics simulations. Theor. Chem. Acc. 103, 124–140.

Loche, P., Steinbrunner, P., Friedowitz, S., Netz, R.R., Bonthuis, D.J., 2021. Transferable ion force fields in water from a simultaneous optimization of ion solvation and ion-ion interaction. J. Phys. Chem. b. 125, 8581–8587.

Manning, C.E., 2018. Fluids of the lower crust: deep is different. Annu. Rev. Earth Planet. Sci. 46, 67–97.

Mantegazzi, D., Sanchez-Valle, C., Driesner, T., 2013. Thermodynamic properties of aqueous NaCl solutions to 1073 K and 4.5 GPa, and implications for dehydration reactions in subducting slabs. Geochim. Cosmochim. Acta 121, 263–290.

McGary, R.S., Evans, R.L., Wannamaker, P.E., Elsenbeck, J., Rondenay, S., 2014. Pathway from subducting slab to surface for melt and fluids beneath Mount Rainier. Nature 511, 338–340.

Myhill, R., Cottaar, S., Heister, T., Rose, I., Unterborn, C., Dannberg, J., Gassmoeller, R., 2023. BurnMan - a Python toolkit for planetary geophysics, geochemistry and thermodynamics. J. Open Source Softw. 8 (87), 5389.

Neumann, M., 1983. Dipole moment fluctuation formulas in computer simulations of polar systems. Mol. Phys. 50, 841–858.

Ohtani, E., 2020. The role of water in Earth's mantle. Natl. Sci. Rev. 7, 224–232.

Ono, S., 2008. Experimental constraints on the temperature profile in the lower mantle. Phys. Earth Planet. Inter. 170, 267–273.

Pan, D., Spanu, L., Harrison, B., Sverjensky, D.A., Galli, G., 2013. Dielectric properties of water under extreme conditions and transport of carbonates in the deep Earth. Proc. Nat. Acad. Sci. 110, 6646–6650.

Panero, W.R., Thomas, C., Myhill, R., Pigott, J.S., Bureau, H., 2020. Dehydration melting below the undersaturated transition zone. Geochem. Geophys. Geosyst. 21, e2019GC008712.

Pankratz, L.B., King, E.G., 1970. High-temperature enthalpies and entropies of chalcopyrite and bornite. U.S. Bureau of Mines Report of Investigations #7435, 10 p.

Pearson, D.G., Brenker, F.E., Nestola, F., McNeill, J., Nasdala, L., Hutchison, M.T., Matveev, S., Mather, K., Silversmit, G., Schmitz, S., Vekemans, B., Vincze, L., 2014. Hydrous mantle transition zone indicated by ringwoodite included within diamond. Nature 507, 221–224.

Pitzer, K.S., 1983. Dielectric constant of water at very high temperature and pressure. Proc. Natl. Acad. Sci. 80, 4575–4576.

Plummer, L.N., Busenberg, E., 1982. The solubilities of calcite, aragonite, and vaterite in CO$_2$-H$_2$O solutions between 0 and 90°C and an evaluation of the aqueous model of the system CaCO$_3$-CO$_2$-H2O. Geochim. Cosmochim. Acta 46, 1011–1040.

Rastogi, A., Ghosh, A., Suresh, S.J., 2011. Hydrogen bond Interactions between water molecules in bulk liquid, Near electrode Surfaces and around ions. In: Moreno-Piraján, J. (Ed.), Thermodynamics: Physical Chemistry of Aqueous Systems. IntechOpen, London.

Resta, R., 2000. Manifestations of Berry's phase in molecules and condensed matter. J. Phys.: Condens. Matter 12, R107.

Rice, J.R., 1992. Fault stress states, pore pressure distributions, and the weakness of the San Andreas fault. In: Evans, B., Wong, T.F. (Eds.), Fault Mechanics and Transport Properties of Rocks. Academic Press Ltd, New York, pp. 475–503.

Rozsa, V., Pan, D., Giberti, F., Galli, G., 2018. Ab initio spectroscopy and ionic conductivity of water under Earth mantle conditions. PNAS 115, 6952–6957.

Sahle, C.J., Sternemann, C., Schmidt, C., Lehtola, S., Jahn, S., Simonelli, L., Huotari, S., Hakala, M., Pylkkänen, T., Nyrow, A., Mende, K., Tolan, M., Hämäläinen, K., Wilke, M., 2013. Microscopic structure of water at elevated pressures and temperatures. Proc. Natl. Acad. Sci. USA 110, 6301–6306.

Schmandt, B., Jacobsen, S.D., Becker, T.W., Liu, Z., Dueker, K.G., 2014. Dehydration melting at the top of the lower mantle. Science 344, 1265–1268.

Schmidt, M.W. and Poli, S., 2013. Devolatilization during subduction. In: Treatise on Geochemistry, second ed. Elsevier Ltd., pp. 669–701.

Schmidt, M.W., Poli, S., 2003. Generation of mobile components during subduction of oceanic crust. Treatise Geochem. 3, 567–591.

Schwager, B., Boehler, R., 2008. H$_2$O: another ice phase and its melting curve. High Press. Res. 28, 431–433.

Schwegler, E., Galli, G., Gygi, F., Hood, R.Q., 2011. Dissociation of water under pressure. Phys. Rev. Lett. 87, 265501.

Shirey, S.B., Wagner, L.S., Walter, M.J., Pearson, D.G., van Keken, P.E., 2021. Slab transport of fluids to deep focus earthquake depths—thermal modeling constraints and evidence from diamonds. AGU Adv. 2, e2020AV000304.

Shock, E.L., Helgeson, H.C., 1988. Calculation of the thermodynamic and transport properties of aqueous species at high pressures and temperatures: correlation algorithms for ionic species and equation of state predictions to 5 kb and 1000°C. Geochim. Cosmochim. Acta 52, 2009–2036.

Shock, E.L., Helgeson, H.C., 1989. Corrections to Shock and Helgeson (1988). Geochim. Cosmochim. Acta 53, 215.

Shock, E.L., Oelkers, E.H., Johnson, J.W., Sverjensky, D.A., Helgeson, H.C., 1992. Calculation of the thermodynamic properties of aqueous species at high pressures and temperatures. J. Chem. Soc. Faraday Trans. 88, 803–826.

Shock, E.L., Sassani, D.C., Willis, M., Sverjensky, D.A., 1997. Inorganic species in geologic fluids: Correlations among standard molal thermodynamic properties of aqueous cations, oxyanions, acid oxyanions, oxyacids and hydroxide complexes. Geochim. Cosmochim. Acta 61, 907–950.

Soper, A.K., 2013. The radial distribution functions of water as derived from radiation total scattering experiments: is there anything we can say for sure? Int. Scholarly Res. Notices, 279463.

Spaldin, N., 2012. A beginner's guide to the modern theory of polarization. J. Solid State Chem. 195, 2–10.

Srinivasan, K.R., Kay, R.L., 1977. The pressure dependence of the dielectric constant and density of acetonitrile at three temperatures. J. Solut. Chem. 6, 357–367.

Suetsugu, D., Inoue, T., Yamada, A., Zhao, D., Obayashi, M., 2006. Towards mapping three-dimensional distribution of water in the transition zone from P-wave velocity tomography and 660-km discontinuity depths. In: Jacobsen, S.D., Van Der Lee, S. (Eds.), Earth's Deep Water Cycle. American Geophysical Union, Washington DC, pp. 237–249.

Sverjensky, D.A., Shock, E.L., Helgeson, H.C., 1997. Prediction of the thermodynamic properties of aqueous metal complexes to 1000 C and 5 kb. Geochim. Cosmochim. Acta 61, 1359–1412.

Sverjensky, D.A., Harrison, B., Azzolini, D., 2014. Water in the deep Earth: the dielectric constant and the solubilities of quartz and corundum to 60kb and 1200°C. Geochim. Cosmochim. Acta 129, 125–145.

Tanger, J.C., Helgeson, H.C., 1988. Calculation of the thermodynamic and transport properties of aqueous species at high pressures and temperatures: revised equations of state for the standard partial molal properties of ions and electrolytes. Am. J. Sci. 288, 19–98.

Thomas, A.M., Nadeau, R.M., Bürgmann, R., 2009. Tremor-tide correlations and near-lithostatic pore pressure on the deep San Andreas fault. Nature 462, 1048–1051.

Tschauner, O., Huang, S., Greenberg, E., Prakapenka, V.B., Ma, C., Rossman, G.R., Shen, A.H., Zhang, D., Newville, M., Lanzirotti, A., Tait, K., 2018. Ice-VII inclusions in diamonds: evidence for aqueous fluid in Earth's deep mantle. Science 359, 1136–1139.

Uematsu, M., Frank, E.U., 1980. Static dielectric constant of water and steam. J. Phys. Chem. Ref. Data 9, 1291–1306.

van Keken, P.E., Hacker, B.R., Syracuse, E.M., Abers, G.A., 2011. Subduction factory: 4. Depth-dependent flux of H$_2$O from subducting slabs worldwide. J. Geophys. Res. 116, B01401.

VandeVondele, J., Hutter, J., 2007. Gaussian basis sets for accurate calculations on molecular systems in gas and condensed phases. J. Chem. Phys. 127, 114105.

VandeVondele, J., Krack, M., Mohamed, F., Parrinello, M., Chassaing, T., Hutter, J., 2005. QUICKSTEP: fast and accurate density functional calculations using a mixed Gaussian and plane waves approach. Comput. Phys. Commun. 167, 103–128.

Wang, W., Walter, M.J., Peng, Y., Redfern, S., Wu, Z., 2019. Constraining olivine abundance and water content of the mantle at the 410-km discontinuity from the elasticity of olivine and wadsleyite. Earth Planet. Sci. Lett. 519, 1–11.

White, L.T., Rawlinson, N., Lister, G.S., Waldhauser, F., Hejrani, B., Thompson, D.A., Tanner, D., Macpherson, C.G., Tkalčić, H., Morgan, J.P., 2019. Earth's deepest earthquake swarms track fluid ascent beneath nascent arc volcanoes. Earth Planet Sci. Lett. 521, 25–36.

Zhang, Z.G., Duan, Z.H., 2005. Prediction of the PVT properties of water over wide range of temperatures and pressures from molecular dynamics simulation. Phys. Earth. Planet. Inter. 149, 335–354.

Zhang, C., Duan, Z., 2009. A model for C–O–H fluid in the Earth's mantle. Geochim. Cosmochim. Acta 73, 2089–2102.

Zhang, C., Sprik, M., 2016. Computing the dielectric constant of liquid water at constant dielectric displacement. Phys. Rev. B 93, 144201.

Zhang, B., Zhao, C., Yoshino, T., 2021. Fe-Mg interdiffusion in wadsleyite and implications for H_2O content of the transition zone. Earth Planet. Sci. Lett. 554, 116672.

Zoback, M.D., Zoback, M.L., Mount, V.S., Suppe, J., Eaton, J.P., Healy, J.H., Oppenheimer, D., Reasenberg, P., Jones, L., Raleigh, C.B., Wong, I.G., Scott, O., Wentworth, C., 1987. New evidence on the state of stress of the San Andreas fault system. Sci. New Series 238, 1105–1111.

Zoback, M.D., Zoback, M.L., Mount, V.S., Suppe, J., Eaton, J.P., Healy, J.H., Oppenheimer, D., Reasenberg, P., Jones, L., Raleigh, C.B., Wong, I.G., Scott, O., Zoback, M.D., Beroza, G.C., 1993. Evidence for a nearly frictionless faulting in the 1989 (M6.9) Loma Prieta, California, earthquake and its aftershocks. Geology 21, 181–185.